Research Square

Preprints are preliminary reports that have not undergone peer review.
They should not be considered conclusive, used to inform clinical practice,
or referenced by the media as validated information.

Multiscale-Biomimetic Lamellar Hydrogel for Full-Thickness Corneal Replacement

Weiyun Shi

weiyunshi@163.com

Eye Institute of Shandong First Medical University https://orcid.org/0000-0003-4106-373X

Jingting Wang

Eye Institute of Shandong First Medical University

Zhen Shi

Eye Institute of Shandong First Medical University

Shang Yang

Shandong Medical and Pharmaceutical University

Zheng Shao

Eye Institute of Shandong First Medical University

Mingxu Li

Eye Institute of Shandong First Medical University

Fuyan Wang

Eye Institute of Shandong First Medical University

Qingjun Zhou

Eye Institute of Shandong First Medical University https://orcid.org/0000-0002-7770-9275

Ting Wang

Eye Hospital of Shandong First Medical University

Long Zhao

Eye Institute of Shandong First Medical University

Article

Keywords: hydrogel cornea, multiscale architecture, asymmetric surface, full-thickness corneal replacement

Posted Date: November 19th, 2026

DOI: https://doi.org/10.21203/rs.3.rs-11505899/v1

License: This work is licensed under a Creative Commons Attribution 4.0 International License.
Read Full License

Additional Declarations: There is **NO** Competing Interest.

Multiscale-Biomimetic Lamellar Hydrogel for Full-Thickness Corneal Replacement

Jingting Wang, Zhen Shi, Shang Yang, Zheng Shao, Mingxu Li, Fuyan Wang, Qingjun Zhou, Ting Wang, Long Zhao*, Weiyun Shi**

J. T. Wang, Z. Shi, Z. Shao, M. X. Li, F. Y. Wang, Q. J. Zhou, L. Zhao, W. Y. Shi
Eye Institute of Shandong First Medical University, State Key Laboratory Cultivation Base, Shandong Key Laboratory of Eye Diseases, Qingdao Key Laboratory of Ophthalmic Implantable and Interventional Medical Materials, School of Ophthalmology, Shandong First Medical University, Qingdao 266071, P. R. China.
*Corresponding authors
E-mail: weiyunshi@163.com (W. Y. Shi); zhaolong@email.sdfmu.edu.cn (L. Zhao)

S. Yang
Shandong Medical and Pharmaceutical University, Yantai 264003, China

*T. Wang
Eye Institute of Shandong First Medical University, Eye Hospital of Shandong First Medical University (Shandong Eye Hospital), State Key Laboratory Cultivation Base, Shandong Key Laboratory of Eye Diseases, School of Ophthalmology, Shandong First Medical University, Jinan 250021, P. R. China
E-mail: wting@sdfmu.edu.cn (T. Wang)

Keywords: hydrogel cornea, multiscale architecture, asymmetric surface, full-thickness corneal replacement

Abstract:

Fabrication of hydrogels that recapitulate the structural, mechanical, and biological cues of native cornea for full-thickness replacement remains a formidable challenge. In this study, a Janus hierarchically lamellar-structured hydrogel is fabricated via bidirectional freeze-casting and in-plane omnidirectional confined assembly. This hydrogel combines properties typically incompatible in conventional artificial corneas, including optical clarity, high water content, robust mechanical strength, and efficient mass transport, while promoting re-epithelialization and suppressing fibroblast adhesion. In a rabbit full-thickness corneal transplantation model, it restores ocular anatomical integrity, accelerates wound healing, reduces postoperative complications, and delivers therapeutic efficacy comparable to that of allogeneic grafts. This low-cost, facile fabrication strategy offers a promising paradigm for construction of high-performance full-thickness corneal substitutes.

1. Introduction

Faithful recapitulation of the structural characteristics, physicochemical properties, and biological functions of native tissues to achieve full-thickness tissue replacement is a long-standing goal in tissue engineering. Hydrogels are attractive candidates for this purpose owing to their extracellular matrix-mimicking characteristics and favorable biocompatibility[1]. The cornea—an avascular transparent tissue—is a highly representative model for developing tissue-engineered hydrogel scaffolds because of its well-standardized transplantation protocols, straightforward monitoring, and quantifiable outcomes.

Over 97% of individuals with corneal blindness (approximately 10 million) lack access to effective treatment due to global donor shortages[2, 3]. Clinically, a substantial proportion of corneal blindness cases involve deep- or full-thickness stromal pathologies. For such diseases, penetrating keratoplasty (PKP, full-thickness replacement) remains the predominant surgical intervention, accounting for over 90% of transplants performed for these indications in the United States[4]. Therefore, there is an urgent unmet clinical need to develop corneal substitutes for PKP.

Over the past few years, advanced biomimetic strategies, including electrospinning[5], 3D printing[6], electric-field-induced assembly[7, 8], and tissue recapitulation[9], have been applied to fabricate corneal scaffolds that effectively promote epithelial and anterior stromal regeneration and restore optical function. Nevertheless, the human corneal endothelium and deep stroma are unable to undergo physiological regeneration following injury[10]. Consequently, these materials are restricted to lamellar keratoplasty, in which they depend on the host stromal bed and endothelium for structural support and functional compensation. Therefore, the use of synthetic materials to replace the biological functions of the corneal stroma and endothelium represents a key strategy for achieving full-thickness corneal transplantation[11]. Notably, a recent study successfully substituted the endothelial layer with a cell-free artificial endothelium and advanced it to human clinical trials[12]. Despite the clear

rationale for synthetic corneal replacement, attaining both epithelial healing and sustained optical clarity is highly challenging. Current clinical and investigational artificial corneal prostheses typically serve only as biologically inert optical substitutes and fail to support epithelial regeneration or mass exchange (Supplementary Table 1). Persistent non-healing, together with the foreign-body response caused by substantial mismatches in mechanical and biophysical properties predispose the eye to severe complications. For instance, for the most widely used Boston keratoprosthesis (a PMMA-based device), the rates of corneal melting, glaucoma, and retroprosthetic membrane formation are 14.5%, 39.3%, and 36.6%, respectively[13].

Achieving full-thickness corneal replacement with hydrogels requires simultaneous recapitulation of the core biophysical properties of the native cornea, including high optical transparency, robust mechanical integrity, long-term hydration homeostasis, and efficient mass transport. However, reconciling these properties in single-phase hydrogel systems is inherently difficult; hence, novel design strategies inspired by the native corneal architecture are required.

The cornea seamlessly reconciles these contradictory properties owing to its sophisticated hierarchical architecture spanning nano-, micro-, and macroscales (Fig. 1a)[14]. The aligned collagen nanofibrils in the stroma minimize light scattering and confer high transparency. Parallel-stacked submicron sheets offer robust mechanical strength. At the microscale, orthogonally arranged lamellae enhance fracture toughness and form interconnected interstitial spaces for nutrient diffusion[15, 16]. On the anterior surface, the felt-like nanotopography of the basement membrane (BM) stably anchors the epithelial cells to establish a protective ocular barrier, while the posterior smooth endothelium preserves interfacial cleanliness and regulates stromal hydration[17, 18]. Despite their considerable promise, precisely recapitulating such intricate multiscale architectures within hydrogels via a versatile, facile fabrication strategy remains a formidable challenge.

This study reports a bidirectional freeze-casting and in-plane omnidirectional confined assembly strategy for fabricating a superstructured full-thickness corneal substitute (SFTC). This hydrogel recapitulates the nanoscale-to-microscale lamellar architecture of the corneal stroma as well as its asymmetric interfacial features (Fig. 1b, c). Owing to this synergistic structure–function integrating design, the SFTC exhibits native-cornea-matched water content, mechanical strength, and excellent in-plane isotropy, while reconciling multiple seemingly incompatible properties such as optical transparency vs. high porosity and pro-healing vs. anti-adhesion. In a rabbit PKP model, SFTC successfully replaced the core functions of the deep stroma and endothelium, supported epithelial regeneration, and maintained high optical clarity, hydration homeostasis, and reliable wound healing without retroprosthetic membrane formation (Fig. 1d). Its therapeutic efficacy was comparable to that of allogeneic transplantation. Overall, the comprehensive performance of SFTC surpasses that of current mainstream corneal substitutes (Fig. 1e, f). The proposed biomimetic assembly strategy represents a promising approach to alleviate the donor shortage and provides a generalizable paradigm for engineering hydrogels with synergistically balanced complex biophysical properties

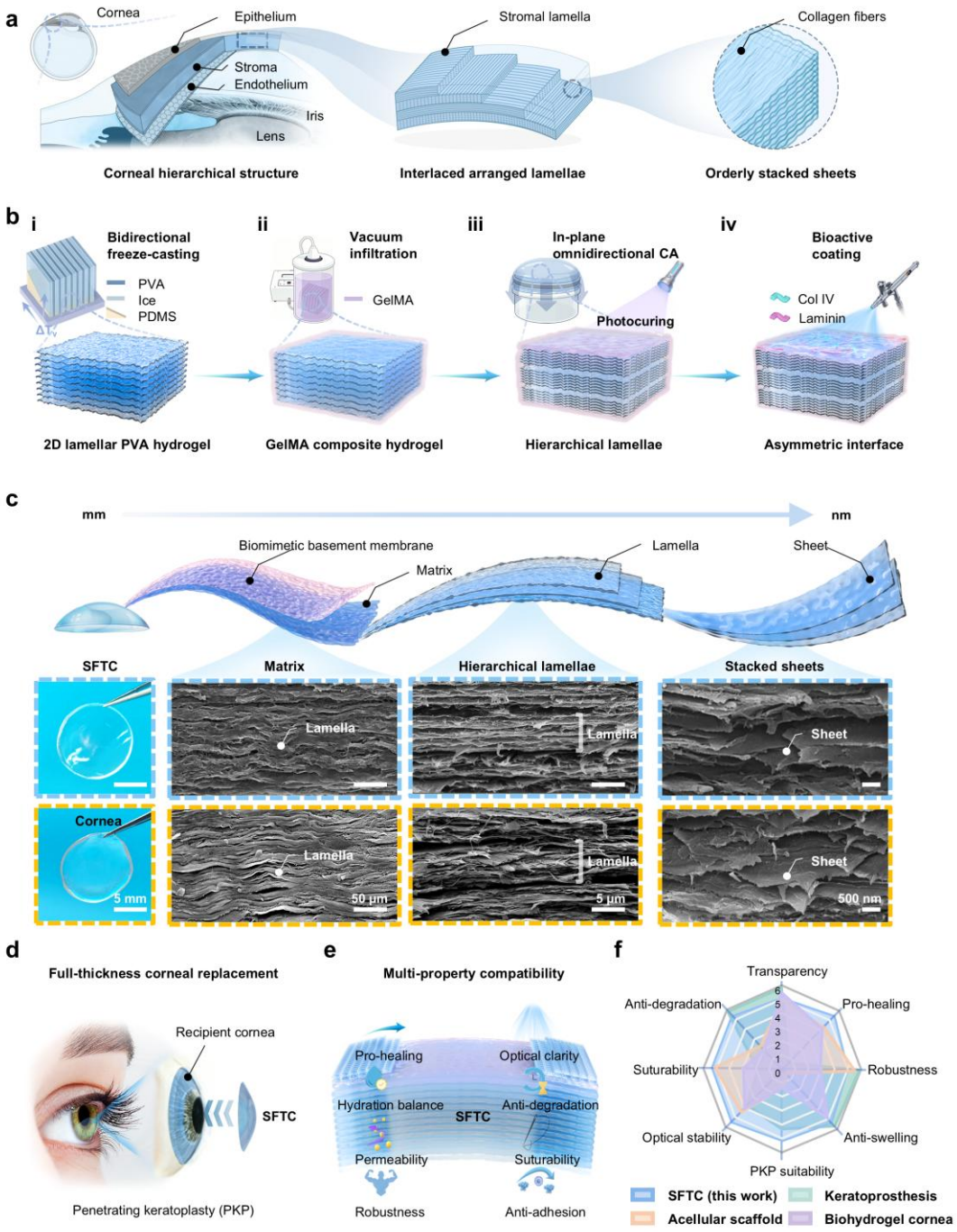


Fig. 1 Fabrication and multifunctional advantages of SFTC. a, Schematic of the spatially layered structures and multiscale hierarchical architectures of the native cornea. **b,** SFTC fabrication workflow involving bidirectional freeze-casting, vacuum-assisted gelatin methacryloyl (GelMA) infiltration, in-plane omnidirectional CA, and bioactive coating. **c,** Multiscale hierarchical structures of SFTC from macroscopic to nano/microscopic levels, compared with native cornea. **d,** Schematic of PKP using

SFTC. **e,** Overview illustrating that SFTC reconciles multiple conventionally competing material properties for full-thickness corneal replacement, with **(f)** each parameter approaching or exceeding those of current clinical and experimental corneal substitutes, including keratoprosthesis, acellular corneal scaffolds, and biomaterial-derived hydrogel corneas, as qualitatively shown in the radar chart. Indices: 1 = poor, 5 = outstanding; detailed evaluation criteria are provided in Supplementary Table 2.

2. Results and Discussion

2.1 Fabrication of SFTC with Hierarchical Multiscale Structures

Two-dimensional (2D) lamellar microstructures were fabricated via bidirectional freeze-casting. Poly(vinyl alcohol) (PVA) was used as the matrix material owing to its excellent biocompatibility and tunable mechanical properties (Fig. 1b-i)[19]. A polydimethylsiloxane (PDMS) wedge with a defined slope was interposed between the PVA precursor solution and cold finger to create a bidirectional temperature gradient throughout the freezing process (Supplementary Fig. 1 and Supplementary Fig. 2). As parallel ice crystals grow along this gradient, PVA polymer chains are progressively excluded into inter-crystalline regions and concentrated therein, promoting formation of interchain hydrogen bonds and thus crosslinking in the polymer network[20]. After sublimation of the ice crystal template, a highly parallel 2D lamellar PVA hydrogel (denoted 2DP) was obtained, with an average interlamellar spacing of 17.5 μm (Supplementary Fig. 3). Furthermore, the lamellar morphology and microstructure could be readily tuned by modulating the fabrication parameters (Supplementary Fig. 4).

The as-prepared 2DP hydrogel was opaque and mechanically weak because its lamellar spacing was an order of magnitude larger than that of the native cornea (Supplementary Fig. 3), leading to severe light scattering and insufficient interlamellar cohesion[21]. Therefore, a simple yet previously unreported assembly

strategy, termed in-plane omnidirectional confined assembly (CA), was developed to replicate the compact lamellar architecture of the cornea (Fig. 1b and Fig. 2a). First, the GelMA prepolymer was infiltrated into the interlamellar voids of 2DP, yielding a composite precursor designated as 2DPG. Subsequently, 2DPG was conformally mounted on a smooth corneal mold, subjected to in-plane omnidirectional pre-strain, photocured for stable fixation onto the mold, and air-dried in situ (Fig. 2a-ii). During drying, water-evaporation-driven shrinkage occurred predominantly along the out-of-plane (vertical) direction, with the in-plane shrinkage highly constrained by strong interfacial adhesion. As the drying front propagated downward from the air-exposed top surface, the adjacent nanosheets converged to form discrete lamellar units via top-to-bottom sequential assembly, yielding a layer-by-layer-stacked micron-scale lamellar framework (Fig. 2a-iii). The resulting hierarchically ordered composite hydrogel was designated as 2DPG-CA. The cured GelMA served as a spacer scaffold that prevented intersheet fusion and structural collapse throughout the process (Supplementary Fig. 5). Owing to sheet densification and the ordered hierarchical assembly, the crystallinity of rehydrated 2DPG-CA increased from 4.8% (2DP) to 17.7% (Supplementary Fig. 6) and the visible-light transmittance increased from 28.7% to 81.0% (Supplementary Fig. 7). 2DPG-CA exhibited an interlamellar spacing of 2.2 μm and an intersheet spacing of 1.1 μm (Fig. 2b and Supplementary Fig. 8), closely matching those of the native cornea (Supplementary Fig. 3).

In addition, the 2DPG-CA hydrogel developed an asymmetric surface topography closely mimicking the structural features of the cornea (Fig. 2c). Groove-like wrinkles were formed on the anterior surface (epi-side) owing to the drying-induced shrinkage stress (Fig. 2d and Supplementary Fig. 9). SFTC was prepared by spray coating type-IV collagen and laminin onto the epi-side with 2DPG-CA as the substrate to recapitulate the biochemical cues of the native BM (Fig. 2a-iii). During the subsequent drying process, the coating spontaneously assembled into nanowrinkled secondary structures with an average spacing of 186 nm—a value within the known feature size range of the BM (20–200 nm)[22] (Fig. 2e and Supplementary Fig. 10). By

contrast, the mold-contacting surface (endo-side) underwent highly constrained volumetric shrinkage, yielding an ultrasmooth morphology (Fig. 2f). Similar to the natural corneal endothelial surface, this endo-side effectively suppressed nonspecific adhesion from the aqueous humor (Fig. 2c), as described in later sections.

H&E staining revealed that the general architecture of SFTC was highly similar to that of the native human cornea (NHC). It comprised a distinct superficial layer and a matrix region exhibiting a wavy, ordered lamellar arrangement (Fig. 2g). Masson's trichrome staining consistently revealed bright blue staining in the matrix region and red staining in the superficial layer, indicating region-specific matrix compactness (Fig. 2h). Immunofluorescence staining further confirmed that type-I collagen was distributed throughout the matrix region in SFTC, while laminin assembled into a continuous linear BM along the superficial layer (Fig. 2i).

The nanoscale structural features of SFTC were examined via small-angle X-ray scattering (SAXS) and wide-angle X-ray scattering (WAXS). GelMA-free 2DP treated with the confined assembly (2DP-CA) and pure GelMA hydrogels were used as controls (Fig. 2j). In the out-of-plane (X–Z) direction, the 2D SAXS patterns of SFTC exhibited distinct diffraction arcs, confirming the preferred orientation of the lamellar architecture (Fig. 2k, m). By contrast, in the in-plane (X–Y) direction, an isotropic scattering halo was observed in the WAXS patterns (Fig. 2l, n). 2DP-CA exhibited nearly flat azimuthally integrated intensity profiles in both directions, which can be attributed to lamellar fusion (Fig. 2m, 2n, and Supplementary Fig. 11). The long-range lamellar order and in-plane isotropy of SFTC were further verified via polarized optical microscopy analysis (Supplementary Fig. 12).

A strong diffraction peak was observed at $2\theta = 19.8°$ in the 1D WAXS profiles of both SFTC and 2DP-CA, assigned to the $(10\bar{1})$ reflection plane of semicrystalline PVA[23] (Fig. 2p). SFTC exhibited a unique peak at $2\theta = 31.1°$ (d-spacing = 2.9 Å) and an interdomain periodic distance of 11.4 nm (Fig. 2o–q and Supplementary Fig. 13). This

spacing is within the typical interchain hydrogen bond length range of 2.8–3.2 Å[24], suggesting locally ordered packing between GelMA and PVA chains. This inference is supported by the blue shift of the amide I band in the Fourier-transform infrared spectra (Supplementary Fig. 14).

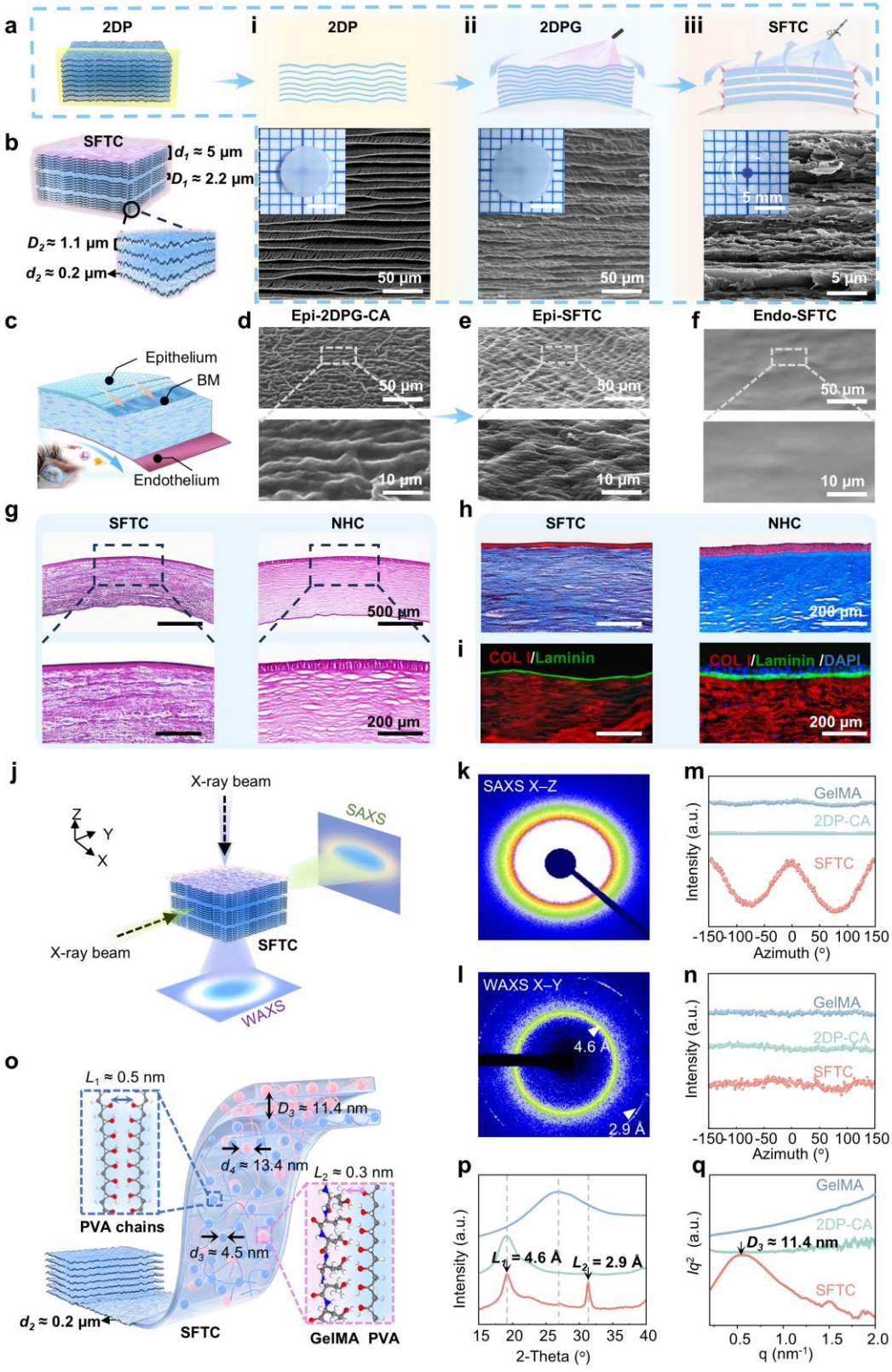


Fig. 2 Design and hierarchical architecture of the SFTC hydrogel. a, Cross-sectional schematic depicting the sheet-assembly mechanism driven by in-plane omnidirectional CA and the corresponding macroscale and ultrastructural features of

the hydrogels. **b,** Hierarchical structural parameters of SFTC: lamellar thickness (d_1), interlamellar spacing (D_1), nanosheet thickness (d_2), and intersheet spacing (D_2). **c,** Asymmetric surface topography of the native cornea: the epithelial side features a nanotextured BM to support cell adhesion, while the endothelial side presents a smooth and clean optical interface. **d–f,** Representative scanning electron microscope (SEM) images of the epi-side of 2DPG-CA **(d)**, SFTC **(e)**, and the endo-side of SFTC **(f)**. **g–i,** H&E staining **(g)**, Masson's trichrome staining **(h)**, and immunofluorescence staining **(i)** results for type-I collagen (red) and laminin (green) in SFTC and NHC. **j,** Schematic of SAXS and WAXS measurements of SFTC with dual orthogonal X-ray incidence. **k–l, (k)** 2D SAXS pattern in the X–Z plane and **(l)** 2D WAXS pattern in the X–Y plane of SFTC. **m–n,** Azimuthal intensity profiles of SAXS **(m)** and WAXS **(n)** for SFTC, 2DP-CA, and GelMA hydrogels. **o,** Nanoscale structural schematic of an SFTC sheet, including intermolecular spacings (L_1, L_2), ordered domain sizes (d_3, d_4), and interdomain periodic distance (D_3). **p,** 1D WAXS intensity profiles. **q,** Lorentz-corrected SAXS intensity profiles.

Collectively, multiscale characterization confirmed that SFTC closely recapitulated the hierarchical architecture of the native cornea, spanning the macroscopic morphology, microscopic lamellar arrangement, and asymmetric surface topography and thereby laying the structural foundation for its biomimetic performance.

2.2 Characterization of Primary Biophysical Properties of SFTC

The optical transparency, hydration stability, mass transport, and degradation resistance of SFTC were systematically characterized, with 2DP, 2DP-CA, 2DPG-RA (randomly assembled 2DPG), and NHC serving as controls. Macroscopically, SFTC and 2DP-CA retained their high transparency and native-cornea-like curvature after rehydration (Fig. 3a). Conversely, 2DPG-RA exhibited severe curling and edge warping induced by the heterogeneous internal stress during drying, while undried 2DP remained completely opaque (Fig. 3a–c).

The equilibrium water content in SFTC was approximately 79.5%, highly similar to that of the native cornea (Fig. 3d). Additionally, SFTC exhibited robust hydration stability, with a swelling ratio below 10% and a negligible transmittance variation after 5 days of incubation in 37 °C physiological saline (Fig. 3e and Supplementary Fig. 15). In contrast, ex vivo NHC underwent drastic swelling (~1000%) and opacification owing to the lack of endothelial integrity (Supplementary Fig. 15). Therefore, whereas native corneas require active endothelial fluid-pumping to drain excess stromal water, the inherently low swelling of SFTC allows for the preservation of graft transparency within the aqueous environment, functionally compensating for the endothelium in preventing graft swelling. 2DPG-RA and 2DP were excluded from subsequent experiments because of their pronounced optical deficiencies.

Being an avascular tissue, the cornea relies primarily on passive diffusion for nutrient supply and metabolic waste removal[25]. The porosity of SFTC was 46.6%, well within the reported range for the native cornea (20%–70%) (Fig. 3f)[26]. The oxygen permeability coefficient (Dk) of SFTC was 67.8 barrer, approximately 2.3-fold that of the native cornea (Fig. 3g). SFTC mimicked the interconnected porous architecture of the native corneal stroma, enabling rapid diffusion via interlamellar voids throughout the scaffold (Fig. 3h). The glucose and lactate permeabilities of SFTC were $6.3 \pm 0.2 \times 10^{-5}$ and $7.0 \pm 0.5 \times 10^{-5}$ cm s^{-1}, respectively, both satisfying the physiological transport requirements of corneas (Fig. 3i–k)[27]. Meanwhile, 2DP-CA, lacking a lamellar architecture, exhibited poor overall permeability.

Owing to the enzymatic stability of the PVA framework, SFTC remained structurally intact after 7 days of collagenase treatment, with no detectable dissolution or fragmentation (Fig. 3l). The SFTC mass loss plateaued at day 3 (final loss, 46.4%, corresponding to the degradable GelMA component), in stark contrast to that of the native cornea (96.8%) (Fig. 3m). Accordingly, after in vivo implantation, SFTC is expected to undergo self-limited degradation, providing a space for extracellular matrix remodeling, while resisting collagenase-mediated graft melting even under

chronic inflammatory conditions.

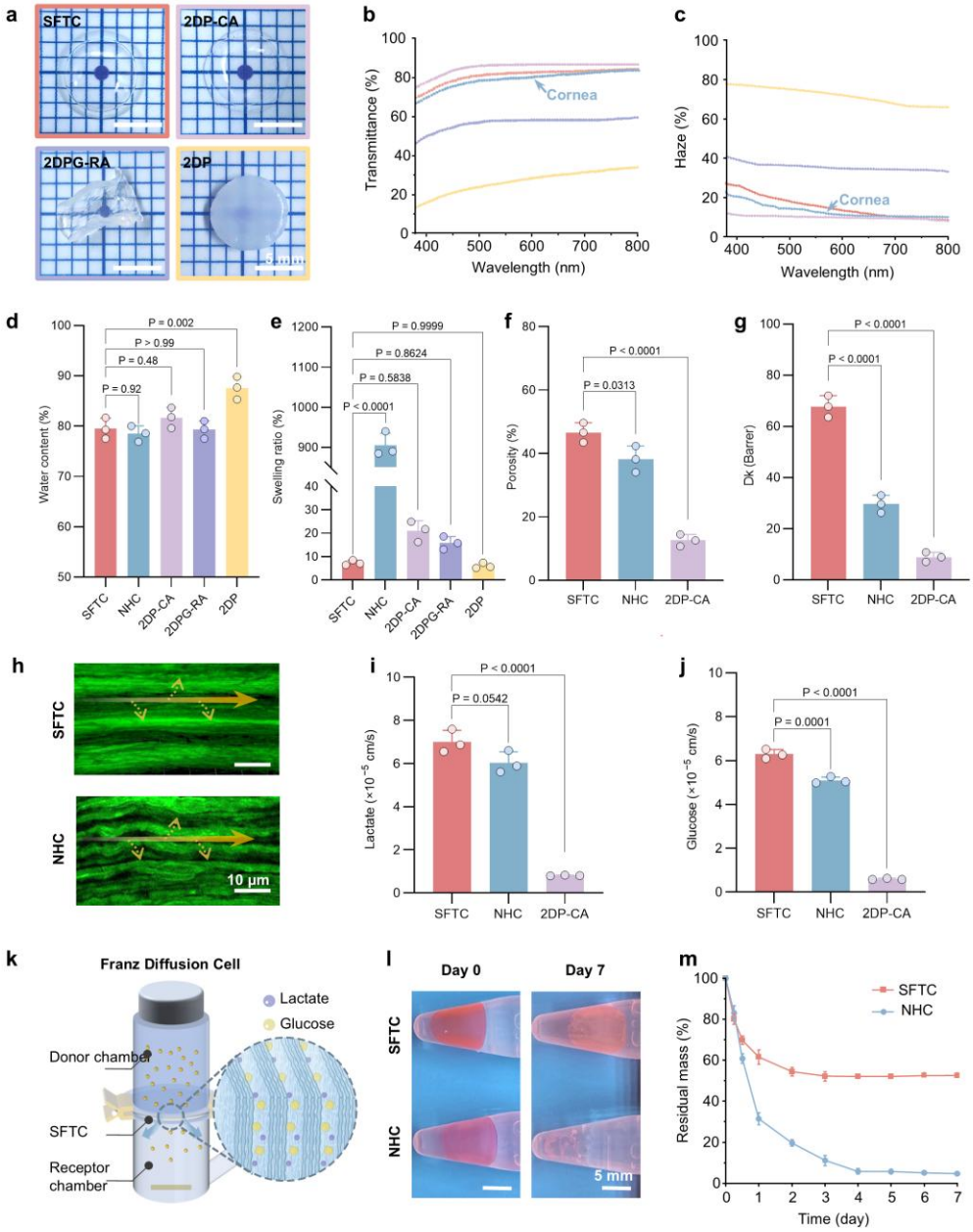


Fig. 3 Optics, hydration, mass transport, and degradation properties of SFTC. a, Macroscopic photographs of SFTC, 2DP-CA, 2DPG-RA, and 2DP. **b, c**, Transmittance (**b**) and haze (**c**) spectra of the hydrogels, with the native cornea as the benchmark. **d**, Water content. **e**, Swelling ratio. **f**, Porosity. **g**, Oxygen permeability (*Dk*). **h**, Immunofluorescence staining for type-I collagen showing the interlamellar spaces in SFTC and NHC; yellow arrows indicate mass transport pathways. **i, j**, Lactate (**i**) and glucose (**j**) permeability coefficients of SFTC, NHC, and 2DP-CA. **k**,

Schematic of the Franz diffusion cell used for in vitro permeation assays. **l**, Macroscopic images and **m**, residual mass curves of SFTC and NHC during 7-day collagenase treatment; samples were stained with 0.2% phenol red for visualization, data are presented as mean ± s.d. (n = 3 independent samples). Statistical significance for **d–g, i, and j** was assessed using one-way ANOVA followed by Tukey's multiple comparisons test; adjusted P values are indicated in the panels. Unless otherwise specified, all statistical tests were two-sided.

2.3 Mechanical Characterization of SFTC

The macroscopic mechanical properties of SFTC were characterized and compared with those of the native cornea and representative corneal substitutes fabricated from PVA (PVA-C)[28], GelMA (Gel-C), and recombinant human collagen (Col-C)[29] (Fig. 4a and Supplementary Fig. 16). The Young's modulus of SFTC (0.81 ± 0.02 MPa) closely matched that of NHC (0.79 ± 0.04 MPa). Furthermore, the toughness of SFTC (1.01 ± 0.16 MJ m^{-3}) was approximately 2.2 times higher than that of the cornea (Fig. 4b, c). SFTC outperformed most of the reported corneal substitutes owing to the combination of favorable stiffness, high toughness, and high water content (Fig. 4d).

Recent studies have demonstrated that constructing preferentially aligned fibrillar architectures effectively improves the mechanical properties of hydrogels[30]. In this study, we hypothesized that generation of 2D lamellar microstructures would endow the hydrogel with superior in-plane isotropic mechanical performance. As shown in Supplementary Fig. 17, SFTC exhibited largely identical tensile stress–strain curves along the two orthogonal in-plane directions, corroborating this prediction. Compared to 1DPG-CA, a hydrogel with uniaxially aligned fibrillar structure, SFTC exhibited comparable tensile strength (1.48 ± 0.21 MPa) parallel to the alignment direction, but a 2.5-fold higher tensile strength perpendicular to the alignment direction (0.60 ± 0.12 MPa) (Supplementary Fig. 17c).

Suture retention testing revealed that SFTC withstood a 200 g load using a 5-0 suture

without visually observable tearing, exceeding the clinical suturing requirements for corneal transplantation[31]. By contrast, the control hydrogels failed to sustain comparable or lower loads (Fig. 4e). Quantitatively, the suture retention strength of SFTC was 23.3 ± 1.3 MPa, which was 2.2-, 23-, and 15.3-fold higher than that of PVA-C, Gel-C, and Col-C, respectively (Fig. 4f). Moreover, the isotropic in-plane suture retention strength of SFTC was 3.0- and 4.6-fold higher than that of 1DPG-CA perpendicular to and along the alignment direction, respectively (Supplementary Fig. 18). Compared with previously reported corneal hydrogels, the SFTC exhibited a superior combination of high suture retention and high water content (Fig. 4g).

Mechanical modeling attributed the enhanced suture retention strength of SFTC to its distinctive lamellar structures, which featured extensive yielding zones and zigzag crack propagation paths (Fig. 4h and Supplementary Fig. 19). As schematically shown in Fig. 4i, the densely stacked lamellae and abundant crystalline domains induced crack-tip blunting and deflection, effectively pinning crack propagation (Supplementary Fig. 20). Beyond this crack-pinning effect, the synergy among interlamellar sliding, sheet pull-out, and interlayer bridging dissipated substantial fracture energy, endowing SFTC with notch insensitivity (Supplementary Fig. 21).

Full-thickness corneal substitutes must tolerate diurnal intraocular pressure (IOP) fluctuations (10–21 mmHg) and acute transient spikes (100–300 mmHg) from routine behaviors, such as squinting and eye rubbing[32]. SFTC delivered an ultimate burst pressure of 445 ± 36 mmHg (Fig. 4j, k), providing a large safety margin. Furthermore, SFTC achieved a fatigue threshold of 580 J m^{-2}, markedly higher than that of PVA-C (104 J m^{-2}), Col-C (19.8 J m^{-2}), and Gel-C (13.2 J m^{-2}) (Fig. 4l). Even after 10,000 tensile cycles at an energy release rate of 520 J m^{-2}, the stress–strain curves of SFTC remained nearly superimposable, with no significant degradation in the mechanical performance (Fig. 4m).

In summary, owing to the rationally designed hierarchical lamellar architecture, SFTC

reconciled typically conflicting mechanical properties of hydrogels, including high strength, high toughness, suture retention, burst resistance, and fatigue resistance while maintaining high water content and in-plane isotropy (Fig. 4n). This exceptional combination of properties can endow SFTC with favorable surgical handling and sustained mechanical compliance after in vivo implantation.

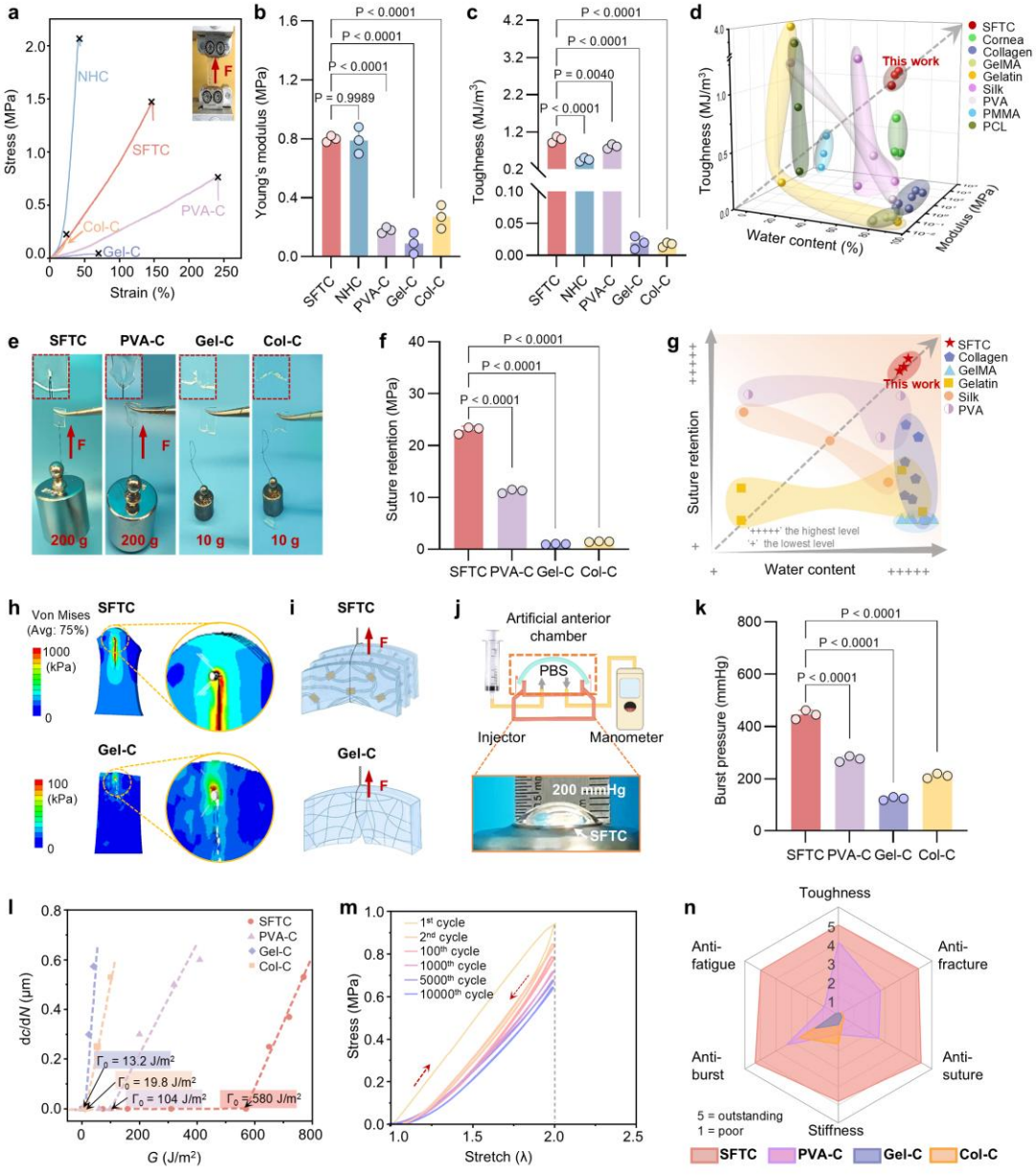


Fig. 4 Mechanical characterization of SFTC. a, Representative stress–strain curves for SFTC, NHC, PVA-C, Gel-C, and Col-C; the inset shows the uniaxial tensile test setup, and black "×" marks indicate fracture points. **b**, Young's modulus and **c**,

toughness of the tested samples. **d**, Ashby plot correlating water content, modulus, and toughness, comparing SFTC with reported corneal substitutes; the dashed line is a guideline for the balance between mechanical properties and hydration performance. **e**, Suture retention under suspended loads for the corneal hydrogels. **f**, Suture retention strength of the tested hydrogels. **g**, Ashby plot of suture retention strength versus water content; the dashed line is a performance balance guideline (appraisal criteria for **d** and **g** are presented in Supplementary Table 3). **h**, Stress nephograms of SFTC and Gel-C under suture tension. **i**, Schematic of the anti-suture-tearing mechanism. **j**, Schematic of the burst pressure test setup. **k**, Ultimate burst pressure. **l**, Crack extension per cycle (dc/dN) versus applied energy release rate (G). **m**, Representative cyclic tensile curves of SFTC over a 10^4-cycle stretching test. **n**, Radar chart comparing core mechanical metrics: toughness, stiffness, suture retention, burst resistance, fracture resistance, and fatigue resistance, data are presented as mean ± s.d. (n = 3 independent samples). Statistical significance for **b, c, f, and k** was assessed using one-way ANOVA followed by Tukey's multiple comparisons test; adjusted P values are indicated in the panels. Unless otherwise specified, all statistical tests were two-sided.

2.4 Cytocompatibility and Biofunction of SFTC

Live/dead fluorescence staining revealed that human corneal epithelial cells (HCECs) and human corneal stromal cells (HCSCs) exhibited intense green and negligible red fluorescence after 48 h of co-culture with SFTC, with the cell viability exceeding 98% (Fig. 5a and Supplementary Fig. 22). The CCK-8 assay confirmed that SFTC exerted no obvious inhibitory effects on cell proliferation (Fig. 5b). Scratch assays revealed accelerated cell migration and wound closure for both HCECs and HCSCs in the SFTC group (Fig. 5c), with over 85% of the wound area repaired within 48 h (Fig. 5d, e).

Immunofluorescence staining demonstrated that HCECs seeded on the SFTC epi-side displayed a typical polygonal cobblestone morphology with robust expression of the

tight junction protein zonula occludens-1 (ZO-1) and corneal-specific marker cytokeratin 3 (CK3). Meanwhile, cells cultured on plates exhibited signs of epithelial-mesenchymal transition (Fig. 5f).

Whole-transcriptome RNA sequencing was performed to elucidate the underlying molecular mechanisms. Principal component analysis (PCA) revealed a clear transcriptomic separation between SFTC-cultured HCECs and plate-grown controls (Fig. 5g). Specifically, 230 differentially expressed genes were identified between the SFTC and control groups (Fig. 5h). Gene ontology (GO) analysis further revealed that the upregulated genes were enriched in biological processes essential for extracellular matrix remodeling and barrier function maintenance, while pathways related to cellular stress and profibrotic signaling were significantly suppressed (Fig. 5i). These transcriptional trends were corroborated via gene set enrichment analysis (GSEA) (Fig. 5j).

The epi- and endo-sides of SFTC exhibited markedly contrasting cell-adhesion behaviors. The density of the adherent HCSCs on the epi-side was approximately 25-fold higher than that on the endo-side (Fig. 5k, m). SEM revealed that HCSCs on the epi-side were well-spread, with abundant filopodia and lamellipodia, and aligned along the groove-ridge topography; by contrast, only sparse, rounded cells with minimal spreading were detected on the endo-side (Fig. 5l and Supplementary Fig. 23). This protein-level adhesion asymmetry was further validated by fibrin-microsphere adhesion, with approximately 90% lower adhesion observed on the endo-side than on the epi-side (Supplementary Fig. 24). This asymmetric adhesion is driven by the Janus surface design, in which ordered nanoscale grooves, pre-coated laminin, and type-IV collagen on the epi-side synergistically create an ideal adhesive microenvironment[33, 34], while the hydrophilic smooth endo-surface resists nonspecific biofouling under aqueous-humor-derived shear stress[35].

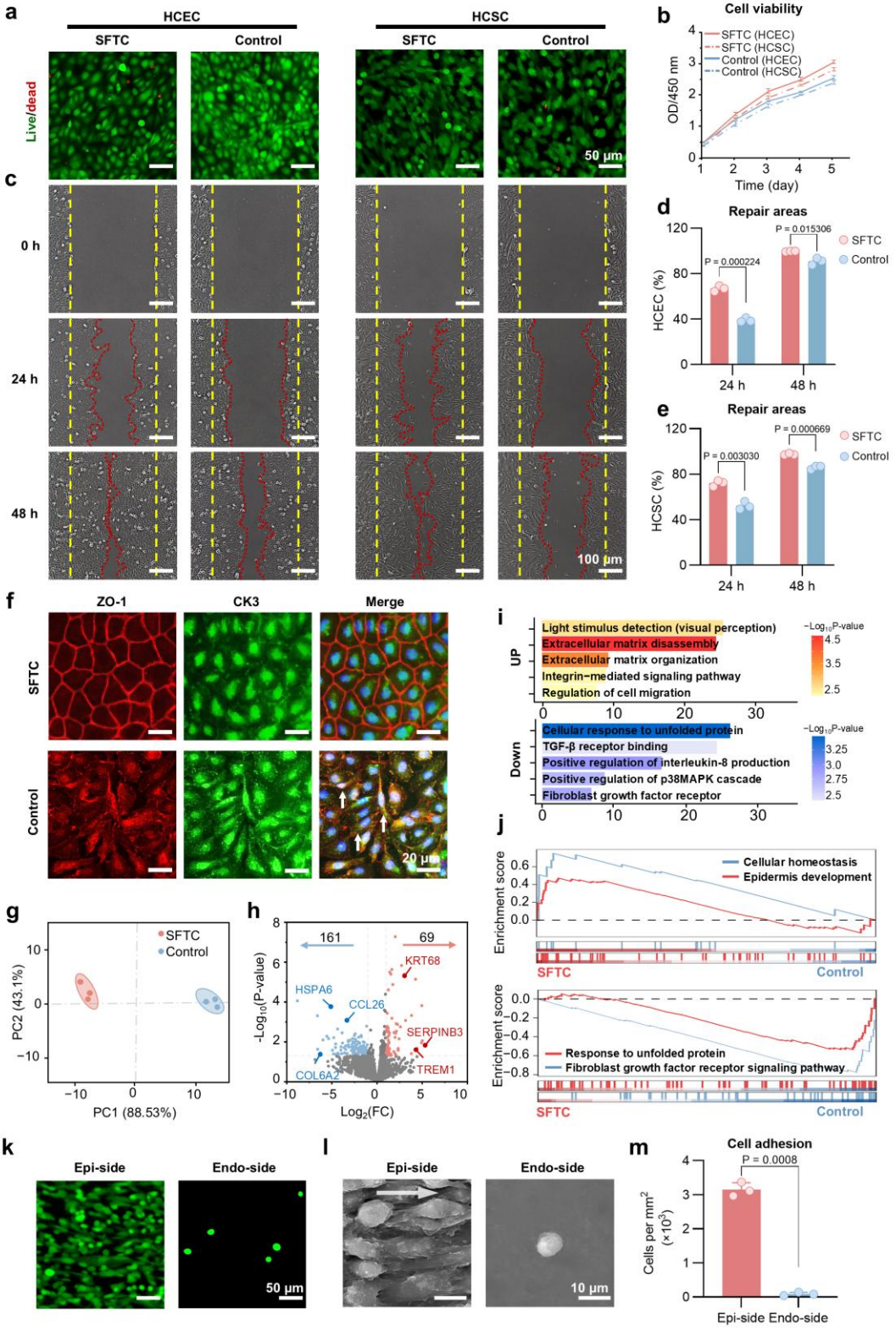


Fig. 5 Cytocompatibility, phenotype preservation, and asymmetric adhesion of SFTC. a, Live/dead staining and **b**, viability curves of HCECs and HCSCs. **c**, Representative scratch assay images and quantified closure rates for **d**, HCECs and **e**, HCSCs at 24 and 48 h post-scratching. **f**, Immunofluorescence staining of ZO-1 and

CK3 in HCECs on the SFTC epi-side versus on a culture plate (control). **g**, PCA of HCEC transcriptomes. **h**, Volcano plot, **i**, GO enrichment, and **j**, GSEA analysis for SFTC versus control. **k**, Fluorescence staining of adherent HCSCs, **l**, SEM images, and **m**, quantification of adherent HCSC density on the epi- and endo-sides, data are presented as mean ± s.d. (n = 3 independent samples). Statistical significance for **d, e, and m** was assessed using two-sided unpaired Student's t-tests; exact P values are indicated in the panels.

2.5 In Vivo Efficacy and Safety of SFTC

Given the combination of the aforementioned biophysical and mechanical properties, SFTC was evaluated as a full-thickness corneal substitute in vivo. As shown in Fig. 6a, a full-thickness corneal injury model was established via high-temperature puncture. Subsequently, a 5.0-mm-diameter corneal trephination was performed to excise the lesional tissue. Thereafter, a 5.25-mm-diameter SFTC graft was implanted and secured using interrupted 10-0 nylon sutures to restore the anatomical integrity of the ocular globe (Fig. 6b). Allogeneic graft (AG) transplantation, PVA-C implantation, and conjunctival flap (CF) coverage—a clinical palliative approach when donor corneas are unavailable[36]—were used as controls.

Slit-lamp examination revealed that SFTC grafts successfully replaced the injured cornea, achieving complete re-epithelialization and maintaining favorable optical transparency over the 28-day follow-up period (Fig. 6c, g, and h). By contrast, the PVA-C group developed persistent epithelial defects, leading to corneal neovascularization and progressive opacity. The CF group achieved perforation closure, but failed to restore transparency. The IOP remained within the physiological range in the SFTC and AG groups at all time points, confirming satisfactory aqueous humor sealing, while transient postoperative hypotony was observed in the PVA-C and CF groups (Fig. 6i).

The anterior segment optical coherence tomography (AS-OCT) results demonstrated

that the matrix density, curvature, and thickness of the SFTC grafts (~400 μm) were comparable to those of AGs (Fig. 6d, f, and k). No evident cellular or fibrinous deposits were detected on the SFTC endo-side, with a stable anterior chamber depth observed during follow-up (Fig. 6j). Meanwhile, abundant fibrinous deposition accompanied by iris synechiae was observed in the PVA-C and CF groups, which resulted in graft opacification and progressive graft thickening (Fig. 6d, k).

Furthermore, in vivo confocal microscopy (IVCM) confirmed that the SFTC grafts induced minimal irritation to the recipient stromal bed: the stromal cell and nerve fiber distributions were comparable to those in the AG group. By contrast, the PVA-C group showed a marked reduction in the keratocyte density with concomitant Langerhans cell infiltration, while in the CF group, abundant hyperreflective spindle-shaped fibroblasts infiltrated the stroma (Fig. 6e).

A cross-modal foraging paradigm was employed to evaluate functional visual recovery (Fig. 6l). The foraging durations and path lengths for SFTC rabbits were comparable to those of the AG group and were significantly shorter than those of all other groups (Fig. 6m, n, and Supplementary Fig. 25).

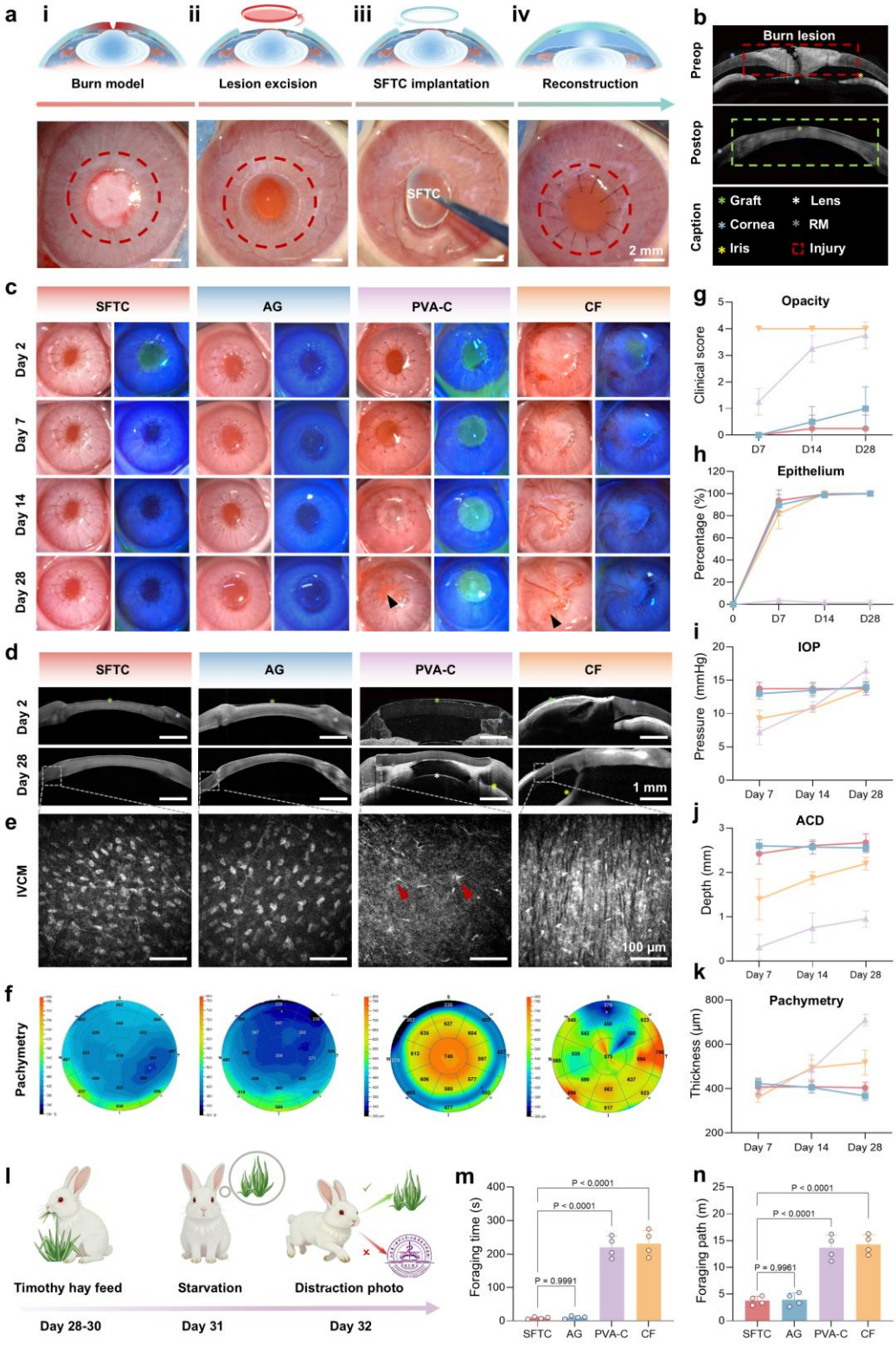


Fig. 6 Therapeutic efficacy of SFTC versus conventional grafts in severe full-thickness corneal injury. a, Schematic and photographs showing the surgical workflow of PKP with SFTC grafts: (i) establishment of the corneal burn model, (ii)

lesioned tissue excision, (iii) SFTC implantation, and (iv) corneal reconstruction and restoration of anatomical integrity. **b**, Representative AS-OCT images of the cornea before and after the intervention; asterisks denote the corresponding anatomical structures: graft (green), cornea (blue), lens (white), iris (yellow), and retrocorneal membrane (RM, magenta). **c**, Representative slit-lamp and fluorescein staining images for the SFTC, AG, PVA-C, and CF groups over the 28-day post-surgery period; the black arrow indicates neovascularization. **d**, Cross-sectional AS-OCT images. **e**, IVCM images of recipient corneas at day 28; the red arrow denotes a Langerhans cell. **f**, Corneal pachymetry maps per group at day 28. **g**, Corneal opacity scores. **h**, Epithelial healing rate. **i**, Intraocular pressure (IOP). **j**, Anterior chamber depth (ACD). **k**, Corneal thickness over the 28-day postoperative period. **l**, Schematic of the visual foraging behavior assay. **m**, Foraging time and **n**, path length for food localization, data are presented as mean ± s.d. (n = 4 animals per group). Statistical significance for **m** and **n** was assessed using one-way ANOVA followed by Tukey's multiple comparisons test; adjusted P values are indicated in the panels. Unless otherwise specified, all statistical tests were two-sided.

Histological staining was performed at the end of the experiments. H&E staining revealed that the structural features of SFTC were highly consistent with those of the surrounding cornea, with a stratified epithelial layer covering the epi-side and no aberrant deposits on the endo-side (Fig. 7a). Meanwhile, the PVA-C group exhibited complete epithelial absence, accompanied by a dense retroprosthetic membrane on the endo-side. The CF group displayed disordered epithelial hyperplasia, with extensive fibroblast infiltration into the stroma.

Immunofluorescence staining confirmed these observations. The SFTC group showed strong, continuous CK3 expression across the epithelial layer, indicating a well-differentiated corneal epithelium (Fig. 7b). α-SMA expression was barely detectable in the SFTC group, indicating that myofibroblast activation was not prominent. Conversely, the PVA-C group exhibited robust α-SMA-positive staining on its endo-

side, confirming the formation of fibrotic retroprosthetic membrane. Moreover, SFTC markedly suppressed CD31-positive neovascularization and CD45-positive inflammatory cell infiltration compared with the PVA-C and CF groups.

Proteomic analysis revealed substantial differences between the protein expression profiles of the SFTC and PVA-C groups (Supplementary Fig. 26). Proteins associated with epithelial adhesion and stability were upregulated in the SFTC group, while fibrosis-related proteins were downregulated (Fig. 7c). Functional enrichment analysis revealed that the pathways involved in wound healing, fibrosis, and inflammation were significantly suppressed in the SFTC group (Fig. 7d), while those related to cell adhesion and epidermal growth factor response were enriched (Fig. 7e). These findings collectively indicate that the SFTC group transitions to the resolution phase of wound healing and restored tissue homeostasis.

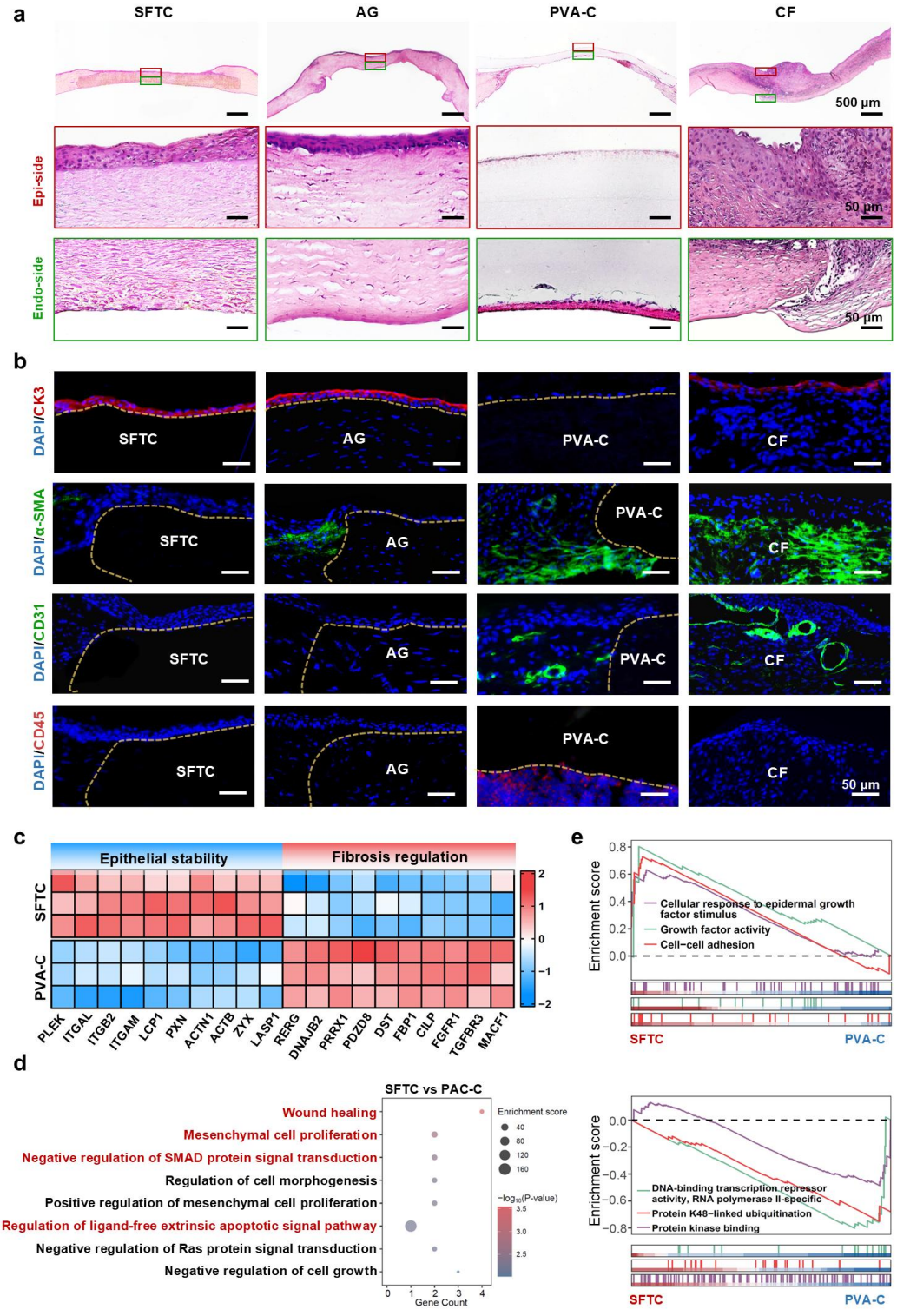


Fig. 7 Histopathological and proteomic analysis of repaired corneas. a, H&E staining of corneas in the different treatment groups, with magnified views of the epi-side (red) and endo-side (green). **b**, Representative immunofluorescence staining for CK3, α-SMA, CD31, and CD45; dashed lines delineate the graft boundary. **c**,

Heatmap of epithelial-stability and fibrogenesis-associated proteins (SFTC vs PVA-C). **d**, GO analysis of upregulated proteins in SFTC. **e**, GSEA plots of representative protein sets. Histological and immunofluorescence images are representative of $n = 4$ corneas per group. Proteomic analyses (**c–e**) were performed with $n = 3$ biological replicates per group; GO enrichment was assessed using Fisher's exact test and GSEA using a permutation-based test, with adjusted $P < 0.05$ considered significant.

Overall, SFTC implantation rapidly restored the globe integrity and corneal optical function. Its favorable wound healing and mild inflammatory response may help mitigate the risk of immune rejection and create favorable conditions for stable degradation and nerve ingrowth, thereby potentially sustaining long-term graft transparency and promoting organized regeneration. However, these promising potentials require further validation through long-term observation and large animal studies. Current evidence indicates that, in scenarios requiring emergent PKP, SFTC holds promise as a ready-to-use, pro-healing, and easily storable acellular substitute, preserving visual function and thereby providing a sufficient time window for patients awaiting donor corneas.

In addition to its robust performance in corneal reconstruction, this SFTC demonstrates potential as a novel visualization platform for dynamic monitoring of disease progression and tissue development. In a mouse model of full-thickness scalp skin replacement, its excellent transparency enabled real-time visualization of the subcutaneous vasculature, while its favorable biocompatibility supported skin regeneration (Supplementary Fig. 27).

3. Conclusion

Using the cornea as a structural blueprint, this study presents a simple yet effective design strategy that couples bidirectional freeze-casting with in-plane omnidirectional confined assembly to fabricate a Janus corneal prosthesis. The scaffold recapitulates the sophisticated multiscale architecture and biochemical cues of the native cornea.

Compared with existing analogs, the resulting SFTC achieves a unique balance among multiple properties typically incompatible with conventional hydrogel systems, including high transparency, high water content, structural robustness, in-plane isotropy, efficient mass transport, and integrated anti-adhesion and pro-regenerative bioactivities. To the best of our knowledge, this is the first report of engineering an acellular hydrogel scaffold capable of promoting wound healing and achieving full-thickness functional replacement in vivo. This low-cost, facile fabrication strategy paves a new avenue for rational design of full-thickness corneal substitutes and holds promise for broader translation to other soft-tissue reconstruction scenarios.

4. Methods

Preparation of 2DP. 5% (w/v) PVA was dissolved in deionized water under stirring at 90 °C for 3 h and degassed via centrifugation. The solution was cast into a square polytetrafluoroethylene (PTFE) mold (40 mm × 40 mm × 40 mm; PTFE sides and a copper base) fitted with a 20°-sloped PDMS wedge at the bottom, with the copper base directly contacting dry ice for freezing at −80 °C. Two full freeze-thaw cycles (12 h freezing at −80 °C, 12 h thawing at room temperature with 55% relative humidity and 24 °C) were then completed.

Preparation of 2DPG-CA. 2DP hydrogels were immersed in a 10% (w/v) GelMA prepolymer solution containing 0.25% (w/v) sodium phenyl (2,4,6-trimethylbenzoyl) phosphinate and vacuum infiltrated for 8 h to yield 2DPG. The resulting 2DPG hydrogels were mounted on a custom-made corneal mold with a curvature of 44 D, prestrained to 10%, secured with an annular clamp, and photo-crosslinked under 365-nm UV irradiation (100 $mW \cdot cm^{-2}$) for 1 min. The samples were then air-dried for 48 h at 24 °C and 20% relative humidity to obtain the 2DPG-CA hydrogels.

Preparation of SFTC. A prepolymer solution containing 0.2 U/mL transglutaminase, 1% (w/v) Col IV, and 0.1% (w/v) laminin was uniformly spray-coated onto the as-

prepared 2DPG-CA hydrogels using an airbrush (ANEST IWATA HB-BP, Japan), followed by incubation at 37 °C for 30 min for transglutaminase-mediated covalent crosslinking, drying at 24 °C and 20% relative humidity for 48 h, equilibration in deionized water, sterilization via ^{60}Co gamma irradiation at 15 kGy (Zhongjin Radiation Technology Co., Ltd., Shenzhen, China), and storage at 4 °C until use.

The preparation protocols for all control hydrogels and detailed procedures for material characterization assays are provided in the Supplementary Information.

Statistical analysis

All statistical analyses were performed using GraphPad Prism 10 (GraphPad Software, San Diego, CA, USA) and Origin Pro 2024b (version 10.1.0.178; OriginLab Corporation, Northampton, MA, USA). Each experiment was independently repeated at least three times unless otherwise specified, and data are shown as mean ± s.d.. Comparisons between two groups were performed using a two-sided unpaired Student's t-test. For comparisons of three or more groups, one-way analysis of variance (ANOVA) followed by Tukey's post hoc multiple comparisons test was applied. A P value < 0.05 was considered statistically significant.

Funding Statements

This work is supported by Shandong Provincial Key Research and Development Plan (2025CXGC020204, 2024CXPT086), National Natural Science Foundation of China (82401318, 82271058, 82571277), Shandong Provincial Outstanding Talent Cultivation Program (Zhufeng Program, Key Research and Development Project) (ZFJH202501), Taishan Scholar Program (tspd20221110), Natural Science Foundation of Shandong Province (ZR2024QC074).

Author Contributions

Jingting Wang: Writing-original draft, Visualization, Validation, Software, Methodology, Investigation, Formal analysis, Project administration,

Conceptualization. **Zhen Shi:** Visualization, Supervision, Writing -review & editing, Investigation. **Shang Yang:** Software, Methodology, Visualization, Investigation**.** **Zheng Shao:** Visualization, Investigation**. Mingxu Li:** Visualization, Investigation. **Fuyan Wang:** Visualization, Investigation. **Qingjun Zhou:** Supervision, Funding acquisition. **Ting Wang:** Supervision, Project administration, Funding acquisition. **Long Zhao:** Conceptualization, Writing-original draft, Visualization, Writing-review & editing, Investigation, Formal analysis, Project administration, Funding acquisition. **Weiyun Shi:** Writing-review & editing, Supervision, Project administration, Funding acquisition, Conceptualization.

Ethical Approval and Informed Consent

Human corneal tissues used in this study were collected and stored at the Eye Bank of the Eye Hospital, Shandong First Medical University. Tissue collection protocols were approved by the Ethics Committee of Shandong Eye Hospital (Approval No. R202403040178), with written informed consent obtained from all donors or legal representatives prior to specimen procurement. All in vivo animal experiments complied with the Association for Research in Vision and Ophthalmology (ARVO) Statement for the Use of Animals in Ophthalmic and Vision Research, with protocols approved by the Ethics Committee of Qingdao Eye Hospital, Shandong First Medical University (Approval No. W2024022700062).

Conflict of Interest

The authors declare no conflict of interest.

Data Availability

All data supporting the findings of this study are available within the main text and the Supplementary Information. Source data for the figures are provided with this paper.

Supplementary Information

Supplementary Information is available from the Online Library or from the author.

References

1. Yang, Y. X. et al. Ultra-durable cell-free bioactive hydrogel with fast shape memory and on-demand drug release for cartilage regeneration. *Nat. Commun.* **14**, 7771 (2023).
2. Whitcher, J. P., Srinivasan, M. & Upadhyay, M. P. Corneal blindness: a global perspective. *Bull. World Health Organ.* **79**, 214–221 (2001).
3. Lei, M. et al. Engineering a functionality-integrated artificial cornea stromal substitute: Janus bio-adhesive implant with a collagen-based multi-scale biomimetic skeleton. *Bioact. Mater.* **51**, 740–757 (2025).
4. Yu, A. C., Spena, R., Pellegrini, M., Bovone, C. & Busin, M. Deep anterior lamellar keratoplasty: current status and future directions. *Cornea* **41**, 539–544 (2022).
5. Sharifi, S. & Sharifi, H. Electrospun-reinforced suturable biodegradable artificial cornea. *ACS Appl. Bio Mater.* **5**, 5716–5727 (2022).
6. Yuan, Y. et al. 3D printing strategies for bioengineering human cornea. *Adv. Healthc. Mater.* **15**, e02767 (2026).
7. Lei, M. et al. Electrical signal initiates kinetic assembly of collagen to construct optically transparent and geometry customized artificial cornea substitutes. *ACS Nano* **16**, 10632–10646 (2022).
8. Wu, K. et al. Glycerol modulated collagen fibril evolution and lamellar organization for biomimetic corneal substitutes construction. *Small* **21**, e2407606 (2024).
9. Zhao, L. et al. Corneal stromal structure-replicating hydrogel patch for sutureless repair of deep anterior-corneal defects. *Biomaterials* **313**, 122754 (2025).
10. Mohan, R. R., Kempuraj, D., D'Souza, S. & Ghosh, A. Corneal stromal repair and regeneration. *Prog. Retin. Eye Res.* **91**, 101055 (2022).
11. Lagali, N. Corneal stromal regeneration: current status and future therapeutic potential. *Curr. Eye Res.* **45**, 278–290 (2020).
12. Zhang, X. Y. et al. Plasma processing of artificial corneal endothelium for the treatment of bullous keratopathy: basic research and clinical application. *Chem. Eng. J.* **507**, 160352 (2025).
13. Priddy, J., Bardan, A. S., Tawfik, H. S. & Liu, C. Systematic review and meta-analysis of the medium- and long-term outcomes of the Boston Type 1 keratoprosthesis. *Cornea* **38**, 1465–1473 (2019).
14. Quantock, A. J. et al. From nano to macro: studying the hierarchical structure of the corneal extracellular matrix. *Exp. Eye Res.* **133**, 81–99 (2015).
15. Meek, K. M. & Knupp, C. Corneal structure and transparency. *Prog. Retin. Eye Res.* **49**, 1–16 (2015).
16. Sun, X. L. et al. Bioinspired tissue transparency: achieving sclera-to-cornea transplantation. *Adv. Sci.* **13**, e14871 (2026).
17. Wilson, S. E., Torricelli, A. A. M. & Marino, G. K. Corneal epithelial basement

membrane: structure, function and regeneration. *Exp. Eye Res.* **194**, 108002 (2020).
18. Jiang, D. et al. Metabolic and redox adaptations of the corneal endothelium: from metabolic plasticity to therapeutic opportunities. *Redox Biol.* **93**, 104148 (2026).
19. Liang, X. X. et al. Polyvinyl alcohol (PVA)-based hydrogels: recent progress in fabrication, properties, and multifunctional applications. *Polymers* **16**, 2755 (2024).
20. Hao, M. et al. Functionally graded surfaces and materials: from fabrication to biomedical applications. *Chem. Rev.* **126**, 2143–2196 (2026).
21. Cai, Y. P. et al. Effect of glycerol on sustained insulin release from PVA hydrogels and its application in diabetes therapy. *Exp. Ther. Med.* **12**, 2039–2044 (2016).
22. Thomasy, S. M., Leonard, B. C., Greiner, M. A., Skeie, J. M. & Raghunathan, V. K. Squishy matters – corneal mechanobiology in health and disease. *Prog. Retin. Eye Res.* **99**, 101234 (2024).
23. Xu, Z. et al. Hierarchically aligned heterogeneous core-sheath hydrogels. *Nat. Commun.* **16**, 400 (2025).
24. Zhou, S. M., Liu, Y. H., Wang, S. J. & Wang, L. Chemical features and machine learning assisted predictions of protein-ligand short hydrogen bonds. *Sci. Rep.* **13**, 13741 (2023).
25. Beebe, D. C. Maintaining transparency: a review of the developmental physiology and pathophysiology of two avascular tissues. *Semin. Cell Dev. Biol.* **19**, 125–133 (2008).
26. Hariharan, P., Nabili, M., Guan, A., Zderic, V. & Myers, M. Model for porosity changes occurring during ultrasound-enhanced transcorneal drug delivery. *Ultrasound Med. Biol.* **43**, 1223–1236 (2017).
27. Yao, X. Y. et al. Membranes for the life sciences and their future roles in medicine. *Chin. J. Chem. Eng.* **49**, 1–20 (2022).
28. Bakhshandeh, H. et al. Poly(ε-caprolactone) nanofibrous ring surrounding a polyvinyl alcohol hydrogel for the development of a biocompatible two-part artificial cornea. *Int. J. Nanomed.* **6**, 1509–1515 (2011).
29. Rafat, M. et al. Bioengineered corneal tissue for minimally invasive vision restoration in advanced keratoconus in two clinical cohorts. *Nat. Biotechnol.* **41**, 70–80 (2023).
30. Luo, W. et al. Recent development of fibrous hydrogels: properties, applications and perspectives. *Adv. Sci.* **12**, e2408657 (2025).
31. Aghaei-Ghareh-Bolagh, B. et al. Optically robust, highly permeable and elastic protein films that support dual cornea cell types. *Biomaterials* **188**, 50–62 (2019).
32. Turner, D. C., Girkin, C. A. & Downs, J. C. The magnitude of intraocular pressure elevation associated with eye rubbing. *Ophthalmology* **126**, 171–172 (2019).
33. Ahearne, M., Fernández-Pérez, J., Masterton, S., Madden, P. W. & Bhattacharjee, P. Designing scaffolds for corneal regeneration. *Adv. Funct. Mater.* **30**, 1908996 (2020).
34. Megaw, R. D., Osei-Bempong, C., Shaharuddin, B. & Ahmad, S. Sequential collagen IV and laminin attachment enriches for human corneal epithelial

progenitors. *Invest. Ophthalmol. Vis. Sci.* **51**, 3762–3770 (2010).
35. Wu, S. M. et al. Introducing antifouling properties onto Janus-like decellularized corneas via graft-from zwitterionic polymers. *J. Polym. Sci.* **63**, 475–485 (2025).
36. Nizeyimana, H. et al. Clinical efficacy of conjunctival flap surgery in the treatment of refractory fungal keratitis. *Exp. Ther. Med.* **14**, 1109–1113 (2017).

Supplementary Files

This is a list of supplementary files associated with this preprint. Click to download.

- SupplementaryInformation.pdf